Supplemental Materials

I. CONVERGENCE TEST FOR THE CALCULATION OF ELECTRON–PHONON COUPLING

In the frozen-phonon method, Q is the normal-mode amplitude (in units of $\text{Å}\sqrt{\text{amu}}$), and its choice directly controls the accuracy of the result. If Q is too small, the energy variation induced by the atomic displacements is negligible; once it falls within the numerical error of the density functional theory (DFT) calculation, the resulting electron–phonon coupling (EPC) matrix elements become dominated by numerical noise. If Q is too large, the atoms leave the harmonic region, so that the harmonic approximation breaks down and higher-order anharmonic terms become necessary. A convergence test is therefore required. We use AA-stacked t-$MoTe_2$ at a twist angle of 5.08° as a prototype and test $Q = 1, 2, 5$, and 10, corresponding to maximum atomic displacements of 0.0048, 0.0097, 0.0242, and 0.0484 Å, respectively. As shown in Fig. S11, the band structure responds linearly to the displacement and the calculated EPC matrix elements remain stable. We therefore adopt $Q = 10$ for all subsequent calculations at all twist angles.

II. CHIRAL PHONONS IN TWISTED TMDS

Twisted bilayer TMDs are intrinsically chiral structures and therefore host chiral phonons. The chirality of these phonons is characterized by their polarization, computed from the expectation value of the phonon circular-polarization operator $\hat{S}^z$ [49]:

$$\hat{S}^z = \sum_{j=1}^{N} \left(|R_j\rangle\langle R_j| - |L_j\rangle\langle L_j| \right), \tag{S1}$$

where N denotes the total number of atoms and j is the atom index. The basis vectors $|R_j\rangle$ and $|L_j\rangle$ correspond to the right- and left-circularly polarized states for the j-th atom, defined as follows:

$$\begin{aligned} |R_1\rangle &= \frac{1}{\sqrt{2}}(1, i, 0, 0, \ldots)^{\mathrm{T}}, \quad |L_1\rangle = \frac{1}{\sqrt{2}}(1, -i, 0, 0, \ldots)^{\mathrm{T}}, \\ |R_2\rangle &= \frac{1}{\sqrt{2}}(0, 0, 1, i, \ldots)^{\mathrm{T}}, \quad |L_2\rangle = \frac{1}{\sqrt{2}}(0, 0, 1, -i, \ldots)^{\mathrm{T}}. \end{aligned} \tag{S2}$$

Based on the expectation value $S^z_{nq} = \langle e_{nq}|\hat{S}^z|e_{nq}\rangle$, a phonon mode is classified as linearly polarized if $S^z_{nq} = 0$, circularly polarized if $S^z_{nq} = \pm 1$, and elliptically polarized if $0 < |S^z_{nq}| < 1$. As shown in Fig. S13, the phonon angular momentum (PAM) texture is concentrated primarily along the Γ–M path [50, 51].

III. PHONON MODES IN TMD MONOLAYERS AND BILAYERS

Monolayer WSe_2 (space group $P\bar{6}m2$, No. 187) lacks inversion symmetry, and its three-atom unit cell gives three acoustic and six optical modes. As shown in Fig. S6c, the frequencies of the acoustic modes are consistently below 150 cm^{-1}, whereas the optical modes exhibit frequencies above 150 cm^{-1}. The three acoustic modes are degenerate at the Γ point with zero frequency, indicating the structural stability of the system. The vibration patterns of these modes correspond to rigid-body translations of the three atoms in the x, y, and z directions. Among the optical branches, there are two pairs of doubly degenerate in-plane phonon modes located at 180 cm^{-1} and 250 cm^{-1}. The first pair exhibits out-of-phase vibrations involving only the Se atoms, while the second pair involves out-of-phase vibrations between the Se and W atoms. The remaining two out-of-plane optical modes possess the highest frequencies. The first mode is characterized by out-of-phase vibrations of the Se atoms, while the second corresponds to out-of-phase vibrations between the Se and W atoms as illustrated in Fig. S6a.

In an R-type TMD bilayer, the number of phonon modes doubles relative to the monolayer due to the doubling of atoms in the unit cell. This stacking configuration lacks inversion symmetry [52] and is associated with the space group $R3m$ (No. 160). The phonon band eigenvalues for this structure are shown in Figs. S6d–S6e. In the low-frequency region (below 150 cm^{-1}), this results in three acoustic modes and three optical modes (often referred to as interlayer modes), as shown in Fig. S6d. The acoustic modes correspond to the rigid-body translation of the entire system, where both layers move in-phase along the x, y, and z directions. As illustrated in Fig. S6b, the three low-frequency

optical modes exhibit out-of-phase vibrations between the two layers. Among these, the two in-plane modes are known as shear modes, corresponding to the lateral sliding of the layers [53–55]. The out-of-plane mode is known as the layer breathing mode (LBM), involving out-of-phase vertical displacement. At the Γ point, the three acoustic modes approach zero frequency, while the shear modes and LBM appear at finite low frequencies (e.g., around 20 cm^{-1}).

IV. MODE MIXING IN THE LAYER BREATHING MODE

In t-WSe_2, the out-of-plane weight of the LBM exceeds 90% at twist angles above 7.34° and decreases to 37% at 2.88°; in t-$MoTe_2$ it remains above 80% for angles larger than 3.89° and above 50% at 2.88°. Decomposing the LBM with the frozen-phonon method shows that the in-plane component produces almost all of the band shifts, while the out-of-plane component has little effect [Fig. S12]; calculations on isolated monolayers give the same result. The stronger in-plane mixing in t-WSe_2 therefore drives a larger band renormalization than in t-$MoTe_2$, and above 7.34°, where the in-plane weight is small, the electronic structure is barely affected.

V. WORKFLOW FOR CALCULATING THE ELECTRON–PHONON COUPLING CONSTANT λ

A. The coupling constant λ and the matrix element g

The mode-resolved EPC constant of a phonon mode $(\mathbf{q}, j)$ can be written as

$$\lambda_{\mathbf{q}j} = \frac{2}{N(E_\mathrm{F})\,\hbar\omega_{\mathbf{q}j}} \sum_{\mathbf{k}mn} \left|g^j_{mn}(\mathbf{k},\mathbf{q})\right|^2 \delta(\varepsilon_{\mathbf{k}+\mathbf{q},m} - E_\mathrm{F})\,\delta(\varepsilon_{\mathbf{k},n} - E_\mathrm{F}), \tag{S3}$$

where $\mathbf{q}$ and j label the phonon wavevector and branch, respectively, with angular frequency $\omega_{\mathbf{q}j}$ and energy $\hbar\omega_{\mathbf{q}j}$, while $\mathbf{k}$ is the electron wavevector and n, m are the band indices of the initial and final electronic states, of energies $\varepsilon_{\mathbf{k},n}$ and $\varepsilon_{\mathbf{k}+\mathbf{q},m}$. Here, E_F is the Fermi energy and $N(E_\mathrm{F})$ the electronic density of states at the Fermi level.

The matrix element $g^j_{mn}(\mathbf{k},\mathbf{q})$ couples the electronic states $(n,\mathbf{k})$ and $(m,\mathbf{k}+\mathbf{q})$ through the phonon-induced change in the Kohn–Sham potential:

$$g^j_{mn}(\mathbf{k},\mathbf{q}) = \langle \psi_{m,\mathbf{k}+\mathbf{q}} | \Delta_{\mathbf{q}j} V_\mathrm{KS} | \psi_{n,\mathbf{k}} \rangle\,. \tag{S4}$$

Here $\psi_{n,\mathbf{k}}$ and $\psi_{m,\mathbf{k}+\mathbf{q}}$ are the Kohn–Sham Bloch wavefunctions of the initial and final electronic states, and $\Delta_{\mathbf{q}j} V_\mathrm{KS}$ denotes the first-order change of the Kohn–Sham potential V_KS produced by displacing the lattice along the phonon mode $(\mathbf{q}, j)$. Resolving the mode into the displacements of the individual atoms κ along Cartesian directions α gives

$$g^j_{mn}(\mathbf{k},\mathbf{q}) = \sum_{\kappa\alpha} \sqrt{\frac{\hbar}{2M_\kappa\omega_{\mathbf{q}j}}}\, e^j_{\kappa\alpha}(\mathbf{q}) \left\langle \psi_{m,\mathbf{k}+\mathbf{q}} \middle| \frac{\partial V_\mathrm{KS}}{\partial \Delta R_{\kappa\alpha}(\mathbf{q})} \middle| \psi_{n,\mathbf{k}} \right\rangle, \tag{S5}$$

where M_κ is the atomic mass, $e^j_{\kappa\alpha}(\mathbf{q})$ is the phonon eigenvector, and $\Delta R_{\kappa\alpha}$ is the physical displacement of atom κ along the Cartesian direction α.

B. From atomic displacements to the normal coordinate Q

We express the atomic displacements through a single mass-weighted normal coordinate $Q_{\mathbf{q}j}$,

$$\Delta R_{\kappa\alpha}(\mathbf{q}) = \frac{e^j_{\kappa\alpha}(\mathbf{q})}{\sqrt{M_\kappa}}\, Q_{\mathbf{q}j}. \tag{S6}$$

Because the phonon eigenvectors are orthonormal, $\sum_{\kappa\alpha} |e^j_{\kappa\alpha}(\mathbf{q})|^2 = 1$, Eq. (S6) gives $\sum_{\kappa\alpha} M_\kappa |\Delta R^j_{\kappa\alpha}(\mathbf{q})|^2 = |Q_{\mathbf{q}j}|^2$: the coordinate $Q_{\mathbf{q}j}$ is the collective amplitude of the whole mode, not the displacement of any single atom. The eigenvector is dimensionless, and $Q_{\mathbf{q}j}$ carries units of $\text{Å}\sqrt{\text{amu}}$.

The chain rule then gives

$$\frac{\partial V_\mathrm{KS}}{\partial Q_{\mathbf{q}j}} = \sum_{\kappa\alpha} \frac{e^j_{\kappa\alpha}(\mathbf{q})}{\sqrt{M_\kappa}}\, \frac{\partial V_\mathrm{KS}}{\partial \Delta R_{\kappa\alpha}(\mathbf{q})}. \tag{S7}$$

With (S7), the sum over atomic displacements collapses into the normal-coordinate form

$$\begin{aligned} g^{j}_{mn}(\mathbf{k},\mathbf{q}) &= \sqrt{\frac{\hbar}{2\omega_{\mathbf{q}j}}}\left\langle \psi_{m,\mathbf{k}+\mathbf{q}}\middle|\frac{\partial V_{\mathrm{KS}}}{\partial Q_{\mathbf{q}j}}\middle|\psi_{n,\mathbf{k}}\right\rangle \\ &= Q_{\mathrm{zpf},j}\left\langle \psi_{m,\mathbf{k}+\mathbf{q}}\middle|\frac{\partial V_{\mathrm{KS}}}{\partial Q_{\mathbf{q}j}}\middle|\psi_{n,\mathbf{k}}\right\rangle, \end{aligned} \tag{S8}$$

where $Q_{\mathrm{zpf},j} = \sqrt{\hbar/2\omega_{\mathbf{q}j}}$ is the zero-point amplitude of the mode. Since $Q_{\mathrm{zpf},j} \propto 1/\sqrt{\omega_{\mathbf{q}j}}$, a soft (low-frequency) mode acquires a larger EPC matrix element for the same potential slope. When $Q_{\mathbf{q}j}$ is expressed in Å$\sqrt{\mathrm{amu}}$ and $\hbar\omega_{\mathbf{q}j}$ in meV, the zero-point amplitude is $Q_{\mathrm{zpf},j} \approx 1.4457/\sqrt{\hbar\omega_{\mathbf{q}j}[\mathrm{meV}]}$.

C. Frozen-phonon evaluation of g and λ

A frozen-phonon distortion measures $\partial V_{\mathrm{KS}}/\partial Q$ directly, so (S8) can be evaluated by finite differences. For a Γ-point mode ($\mathbf{q} = 0$), we fix a small amplitude Q and build the two distorted structures

$$\Delta R^{(\pm)}_{\kappa\alpha} = \pm\frac{Q}{\sqrt{M_\kappa}}\, e^{j}_{\kappa\alpha}. \tag{S9}$$

The derivative $\partial V_{\mathrm{KS}}/\partial Q$ can then be evaluated from these two structures by a central finite difference, $\partial V_{\mathrm{KS}}/\partial Q \approx [V_{\mathrm{KS}}(+Q) - V_{\mathrm{KS}}(-Q)]/2Q$, so that (S8) takes the form

$$g^{j}_{mn}(\mathbf{k},\Gamma) \approx Q_{\mathrm{zpf},j}\left\langle \psi_{m,\mathbf{k}}\middle|\frac{V_{\mathrm{KS}}(+Q) - V_{\mathrm{KS}}(-Q)}{2Q}\middle|\psi_{n,\mathbf{k}}\right\rangle. \tag{S10}$$

In a moiré system the topmost valence band is essentially isolated; at half filling the Fermi level lies at the M point, where it is the only band present, so the diagonal term $m = n$ suffices. By the Hellmann–Feynman theorem, $\partial\varepsilon_{\mathbf{k},n}/\partial Q = \langle\psi_{n,\mathbf{k}}|\partial V_{\mathrm{KS}}/\partial Q|\psi_{n,\mathbf{k}}\rangle$, so this diagonal element reduces to a difference of band eigenvalues,

$$g^{j}_{nn}(\mathbf{k},\Gamma) \approx Q_{\mathrm{zpf},j}\,\frac{\varepsilon_{\mathbf{k},n}(+Q) - \varepsilon_{\mathbf{k},n}(-Q)}{2Q}. \tag{S11}$$

For $\mathbf{q} = 0$ and $m = n$, the off-diagonal contributions in (S3) vanish and the two δ functions share the same argument. Equation (S3) then reduces to

$$\lambda_j = \frac{2}{N(E_{\mathrm{F}})\,\hbar\omega_j}\sum_{\mathbf{k}n}\left|g^{j}_{nn}(\mathbf{k},\Gamma)\right|^2\delta(\varepsilon_{\mathbf{k},n} - E_{\mathrm{F}})\,\delta(\varepsilon_{\mathbf{k},n} - E_{\mathrm{F}}), \tag{S12}$$

where $N(E_{\mathrm{F}})$ is the electronic density of states at the M point for half filling.

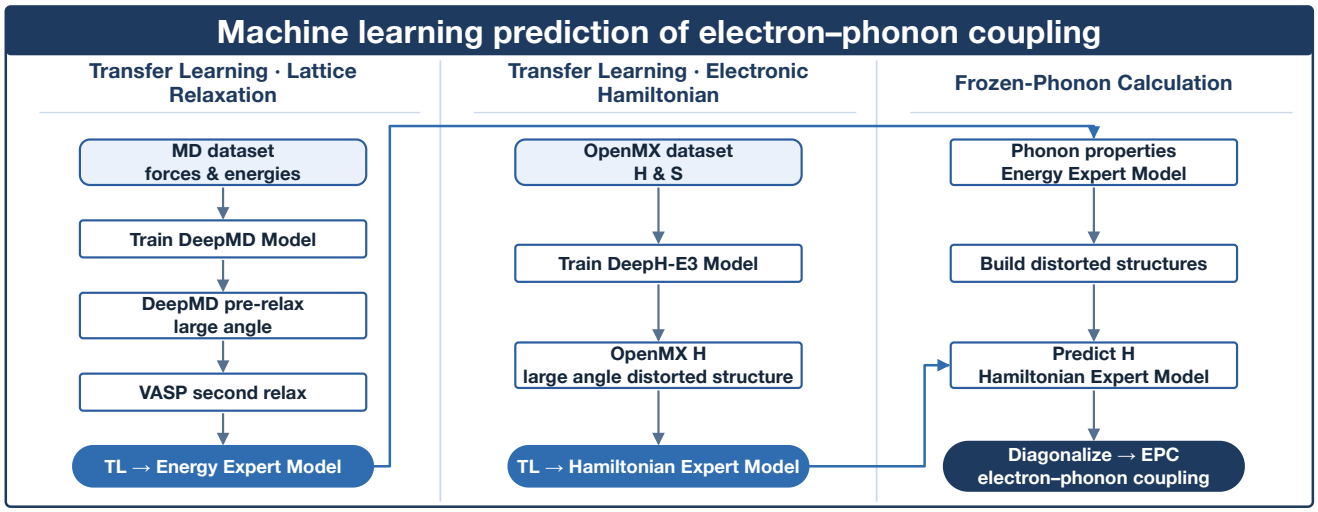

FIG. S1. Workflow of the machine-learning-accelerated calculation of electron–phonon coupling (EPC). The scheme comprises three main procedures, shown as three columns: transfer-learning lattice relaxation, transfer-learning electronic Hamiltonian, and frozen-phonon calculation. In the first procedure, an initial dataset is generated from the non-twisted structure via molecular dynamics (MD) simulations and used to train a coarse DeepMD model. This model provides a preliminary relaxation of the large-angle twisted structure, which is not yet fully relaxed. A second structural optimization is then performed with VASP, and the energies and forces collected along the ionic relaxation steps are used for transfer learning to obtain the Energy Expert Model. In the second procedure, OpenMX is used to compute the Hamiltonian of the non-twisted structure, which serves to train a DeepH-E3 model. An additional dataset of large-angle distorted structures is subsequently incorporated, and transfer learning yields the Hamiltonian Expert Model. In the third procedure, the Energy Expert Model is used to evaluate the phonon properties, and the displacement patterns of individual phonon branches are applied to generate the distorted structures. The Hamiltonian Expert Model then predicts the Hamiltonians of these distorted structures, and their diagonalization gives the phonon-resolved EPC strength.

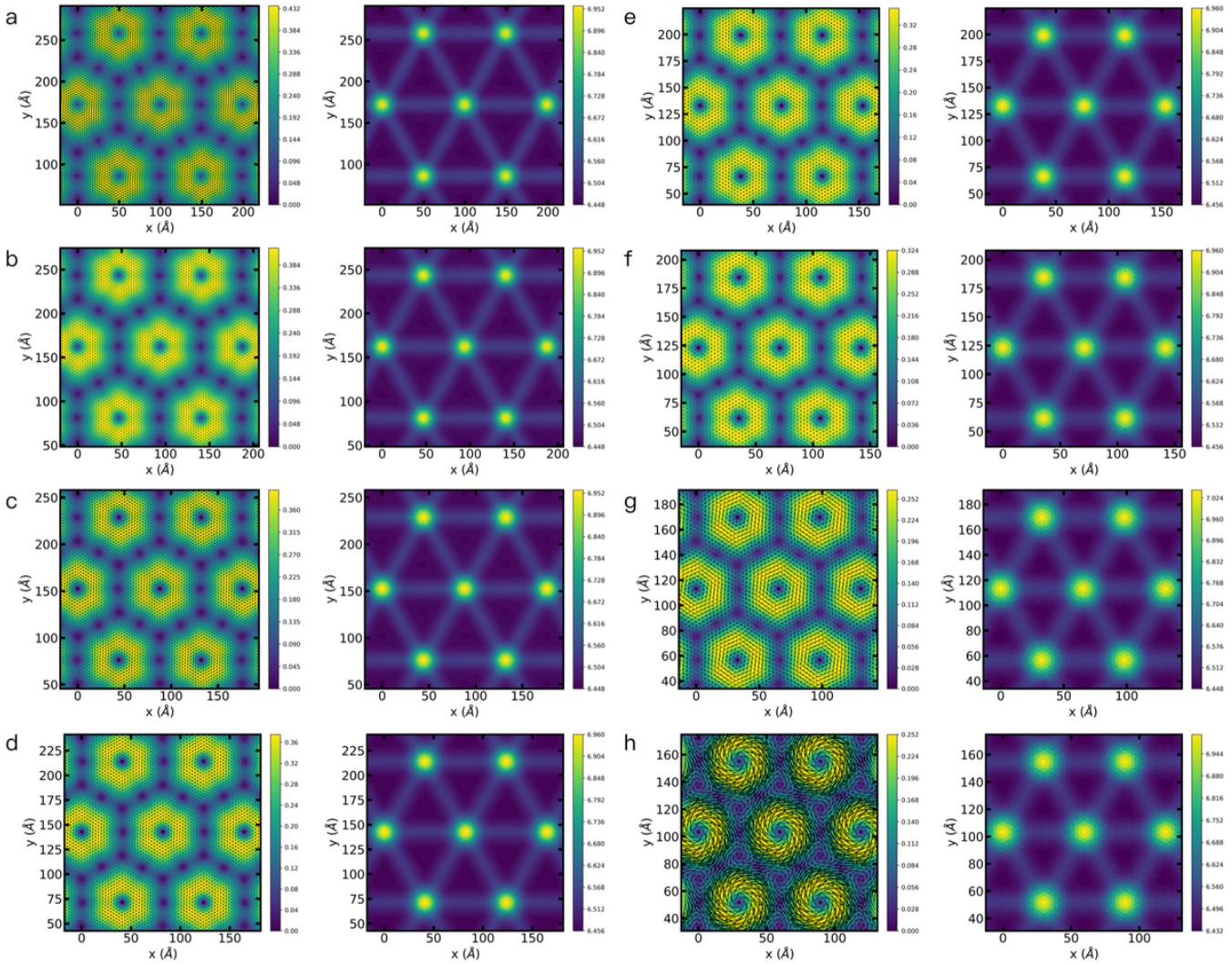

FIG. S2. **a**–**h**, Structural relaxation of AA-stacked t-WSe_2 from 3.15° down to 1.89°. Left panels: Intralayer in-plane displacements of the top-layer W atoms. Right panels: Interlayer distance distribution, calculated as the vertical separation between W atoms in adjacent layers.

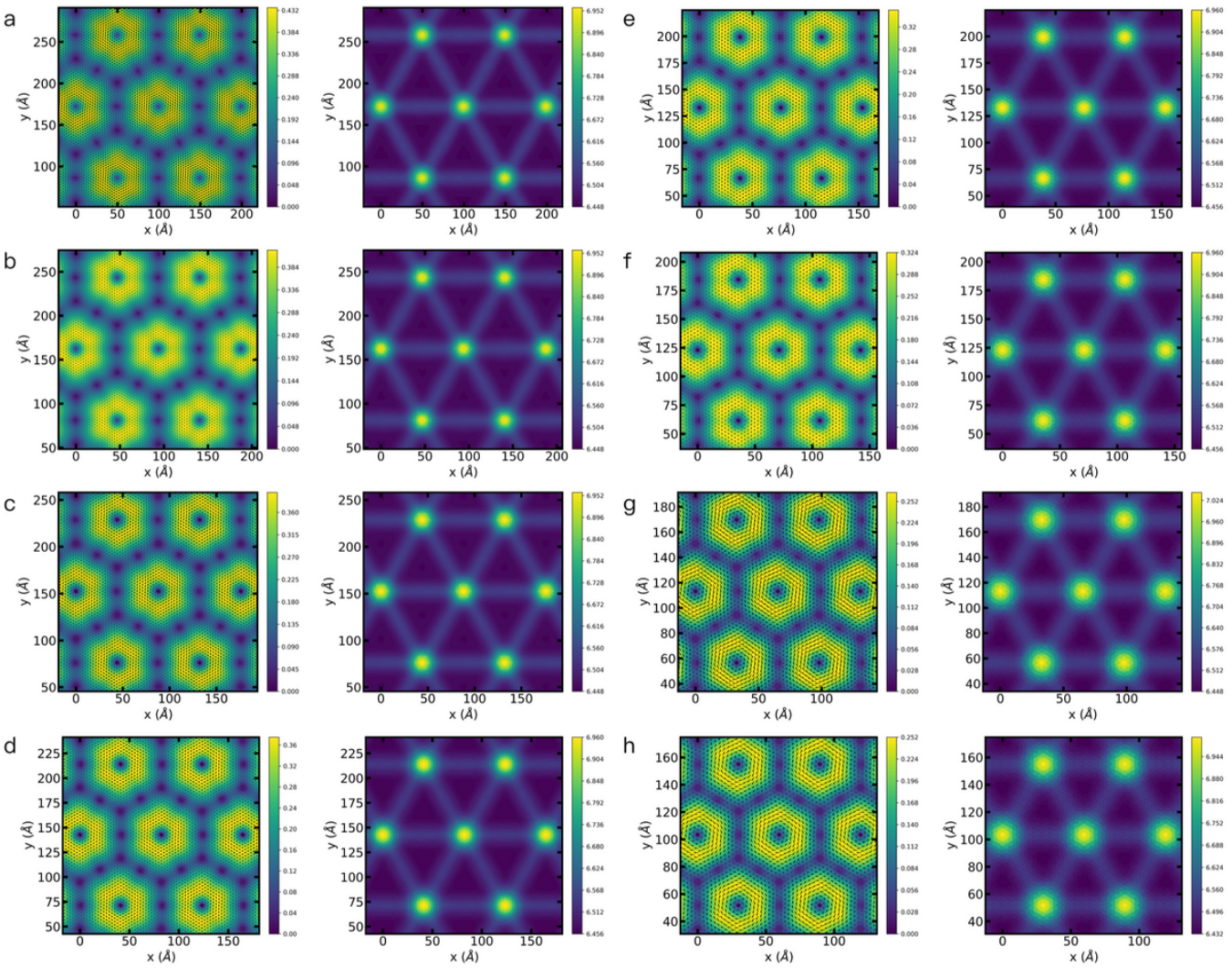

FIG. S3. **a**–**h**, Structural relaxation of AA-stacked t-WSe_2 across twist angles of 3.48°–22°. Left panels: Intralayer in-plane displacements of the top-layer W atoms. Right panels: Interlayer distance distribution, calculated as the vertical separation between W atoms in adjacent layers.

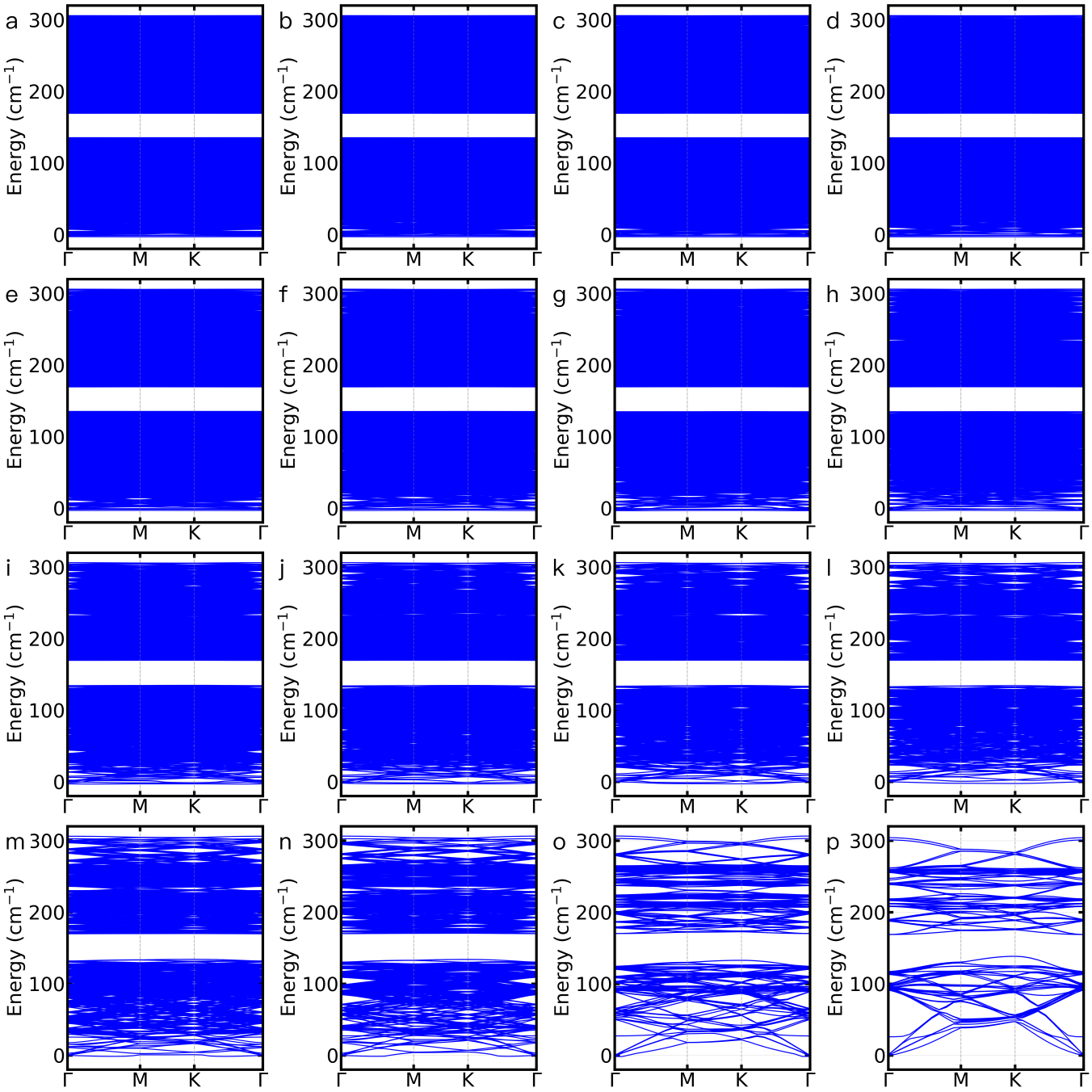

FIG. S4. **a**–**p**, The phonon band structures of AA-stacked t-WSe_2 across twist angles of 1.89°–22°.

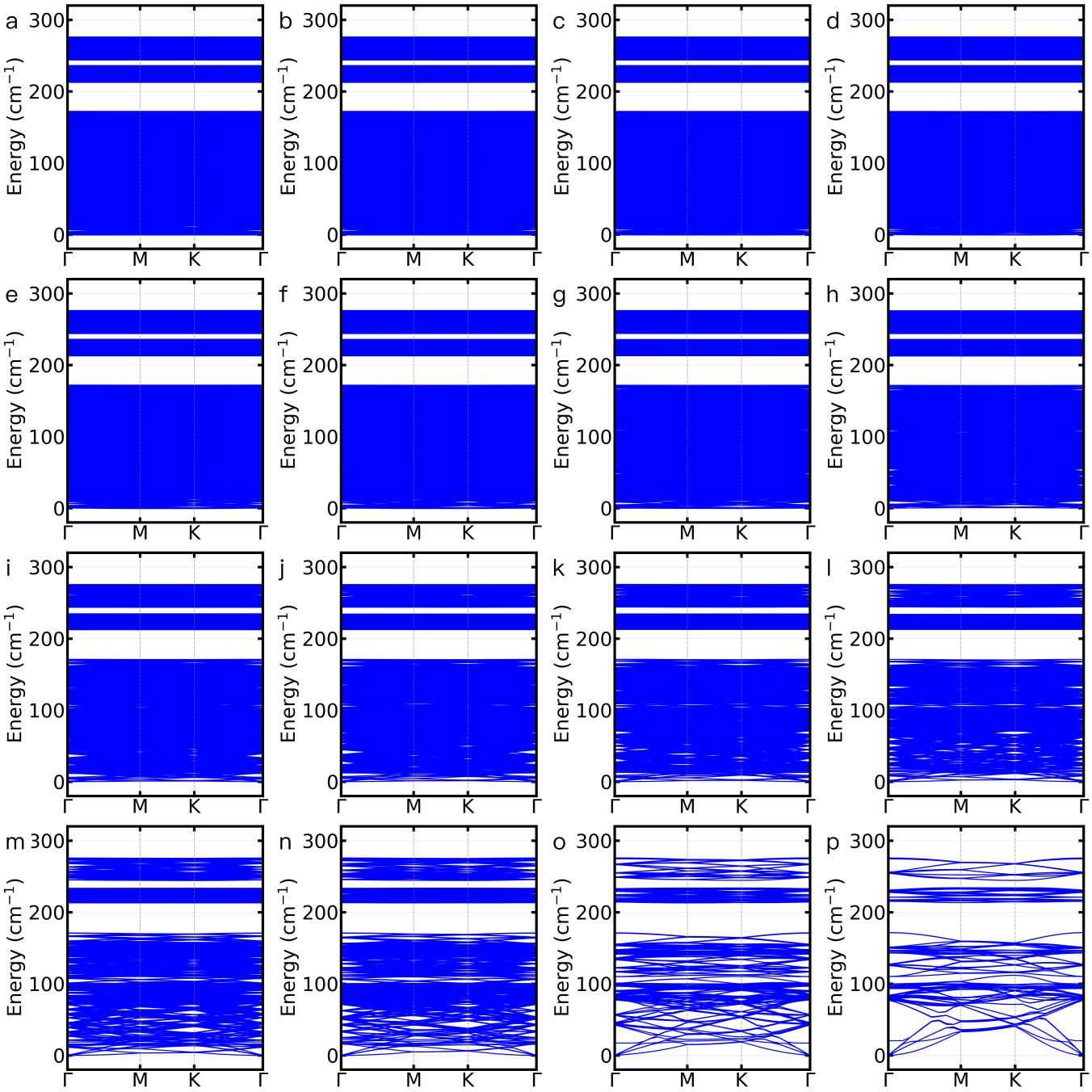

FIG. S5. **a**–**p**, The phonon band structures of AA-stacked t-$MoTe_2$ across twist angles of 1.89°–22°.

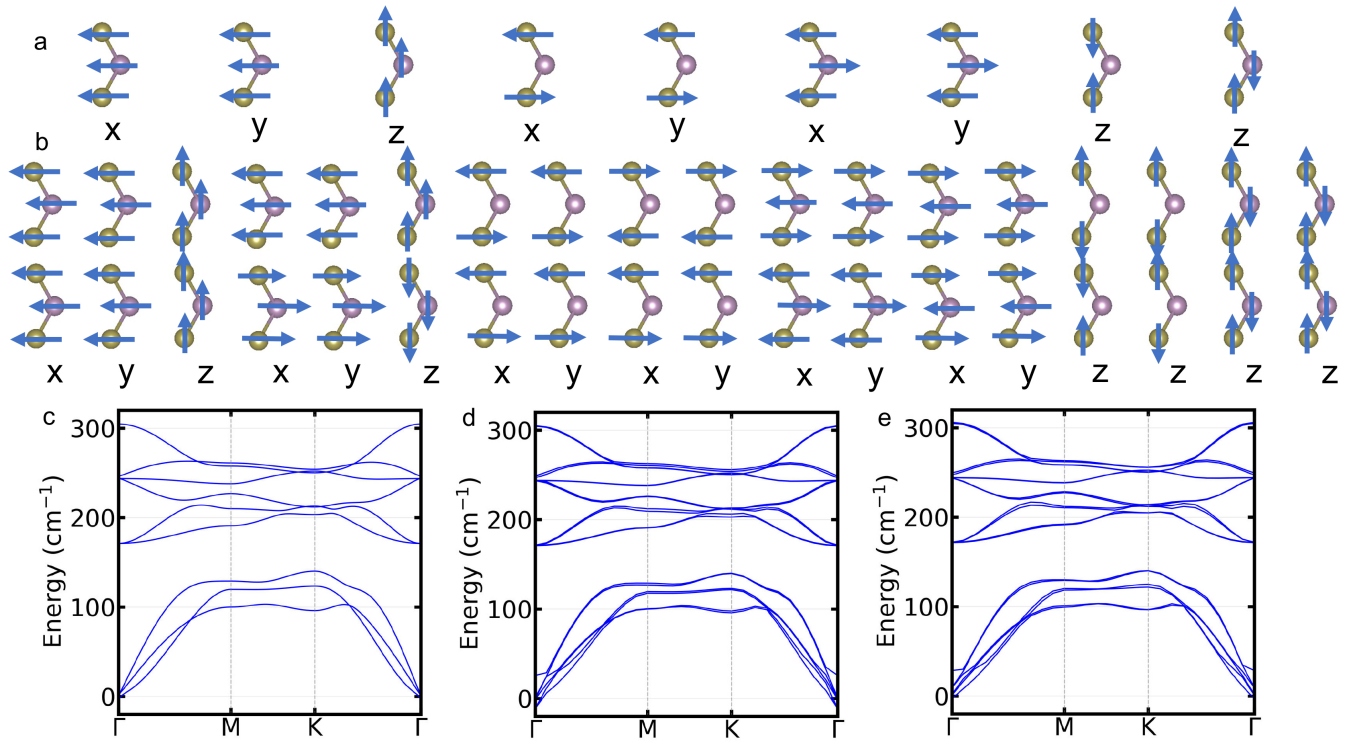

FIG. S6. **a**, Vibrational displacement patterns of the 9 phonon modes in monolayer WSe_2. **b**, The 18 phonon modes of R-type bilayer WSe_2. Arrows indicate the direction of vibration, with x, y, and z representing the polarization axes. The modes are indexed from left to right. **c**–**e**, Phonon band structures of (**c**) monolayer WSe_2, (**d**) R-type bilayer WSe_2, and (**e**) H-type bilayer WSe_2.

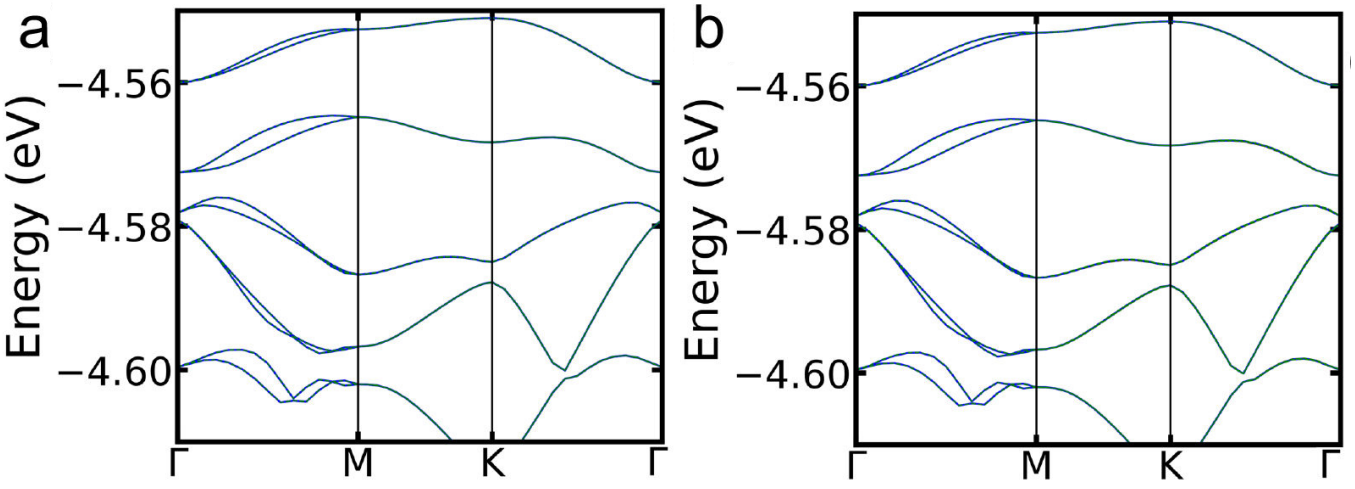

FIG. S7. **a**–**b**, Electronic band structures of t-$MoTe_2$ under different phonon distortions: **a**, acoustic mode, and **b**, layer shear mode.

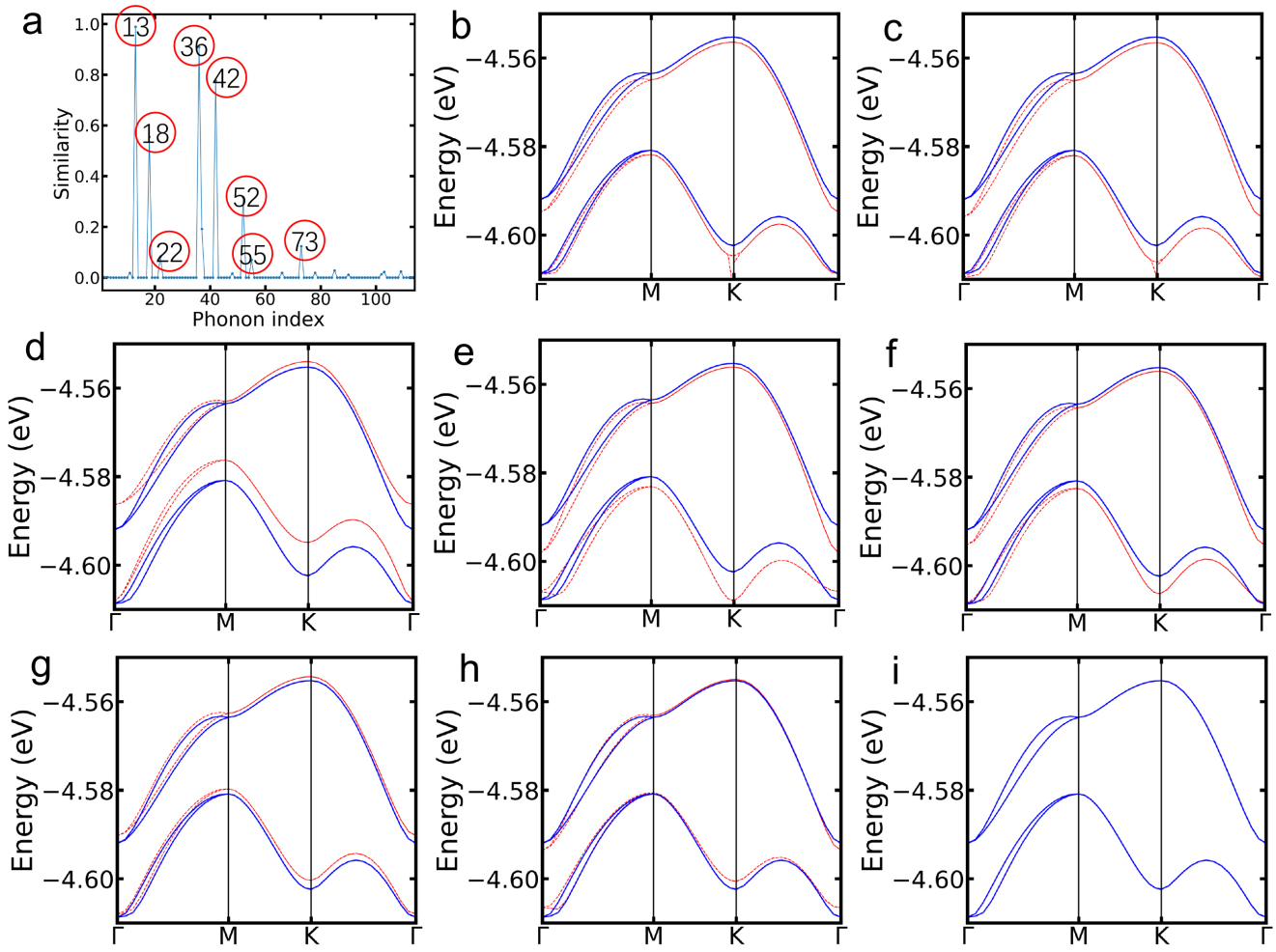

FIG. S8. **a**, Similarity metric for t-$MoTe_2$ at a twist angle of 5.08°. **b**–**i**, Electronic band structures under lattice distortions corresponding to phonon modes with indices 13, 18, 22, 36, 42, 52, 55, and 73, respectively.

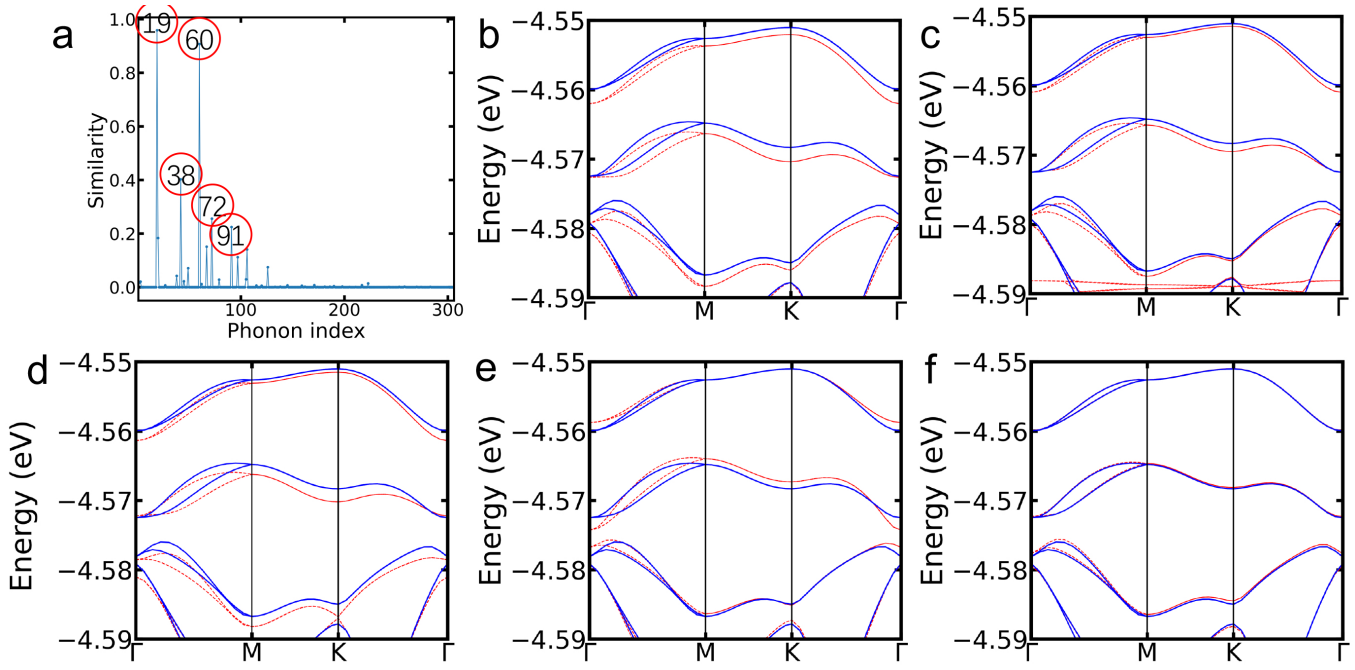

FIG. S9. **a**, Similarity metric for t-$MoTe_2$ at a twist angle of 3.15°. **b**–**f**, Electronic band structures under lattice distortions corresponding to phonon modes with indices 19, 38, 60, 72, and 91, respectively.

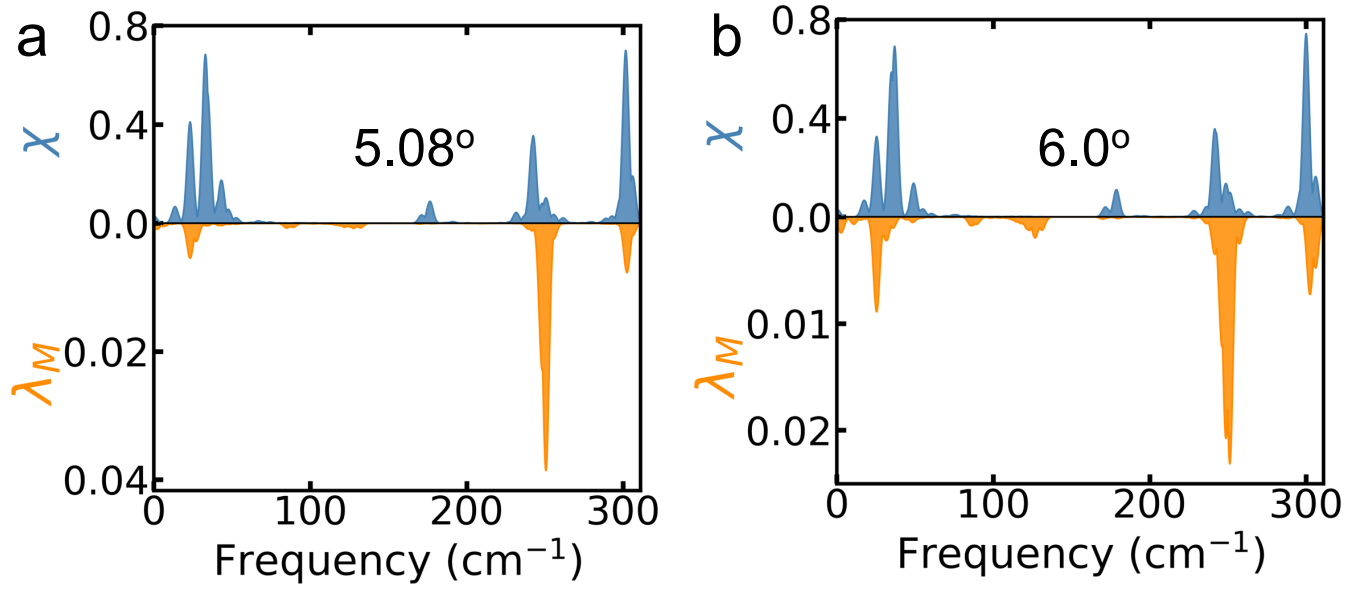

FIG. S10. Frequency-resolved phonon analysis of t-WSe_2. **a**, **b**, Results for twist angles of 5.08° and 6.00°, respectively. In each panel, the upper plot shows the mode-resolved similarity $\chi(\omega)$, while the lower plot shows the corresponding electron–phonon coupling strength $\lambda_M(\omega)$. In the low-frequency region, χ exhibits two pronounced peaks: the first originates from the LBM and is associated with a large λ_M, indicating strong coupling at the M point; the second peak, while having a negligible effect at M, strongly modifies the electronic structure at the Γ point. In the high-frequency region, the two prominent χ peaks both coincide with sizable λ_M peaks.

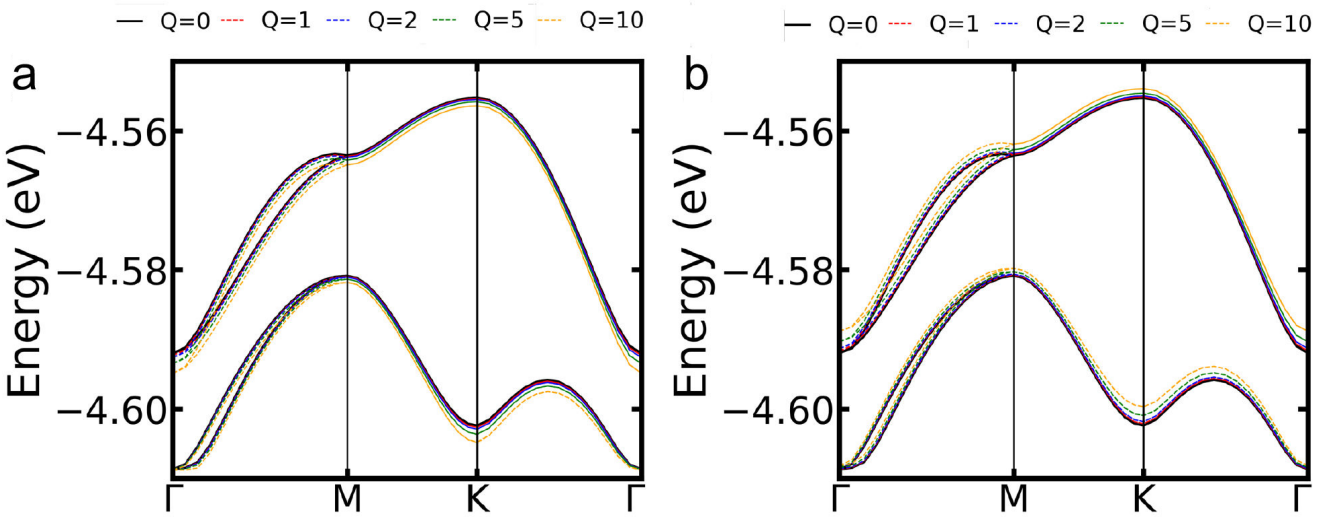

FIG. S11. Electronic band structures calculated for different distortion magnitudes Q. The panels correspond to **a**, positive distortions with $Q = 0, 1, 2, 5, 10$ and **b**, negative distortions with $Q = 0, -1, -2, -5, -10$.

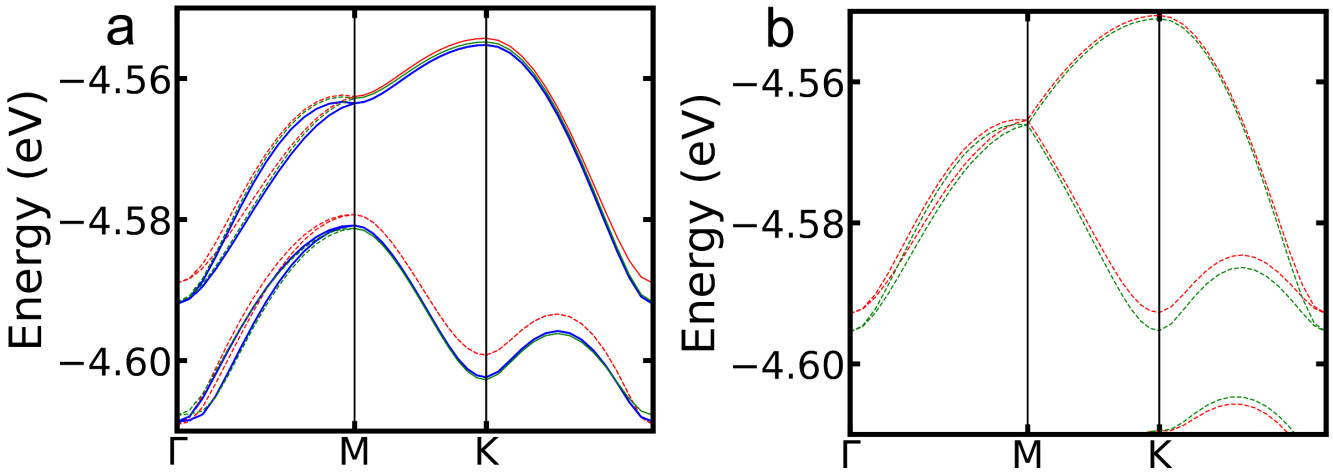

FIG. S12. Electronic band structures of t-$MoTe_2$ modulated by the LBM. **a**, Band structures of the full bilayer system. **b**, Band structures calculated for the isolated upper layer treated as a monolayer. In both panels, blue curves represent the undistorted bands. Red and green curves correspond to the band structures calculated with only the in-plane and out-of-plane displacement components of the LBM, respectively.

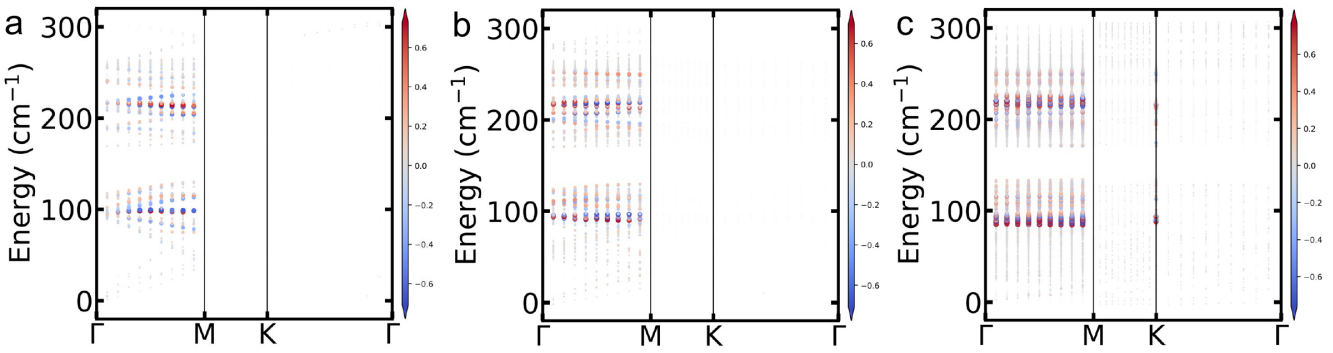

FIG. S13. Chiral phonons in (**a**) untwisted bilayer WSe_2 and t-WSe_2 at twist angles of (**b**) 13° and (**c**) 1.89°.

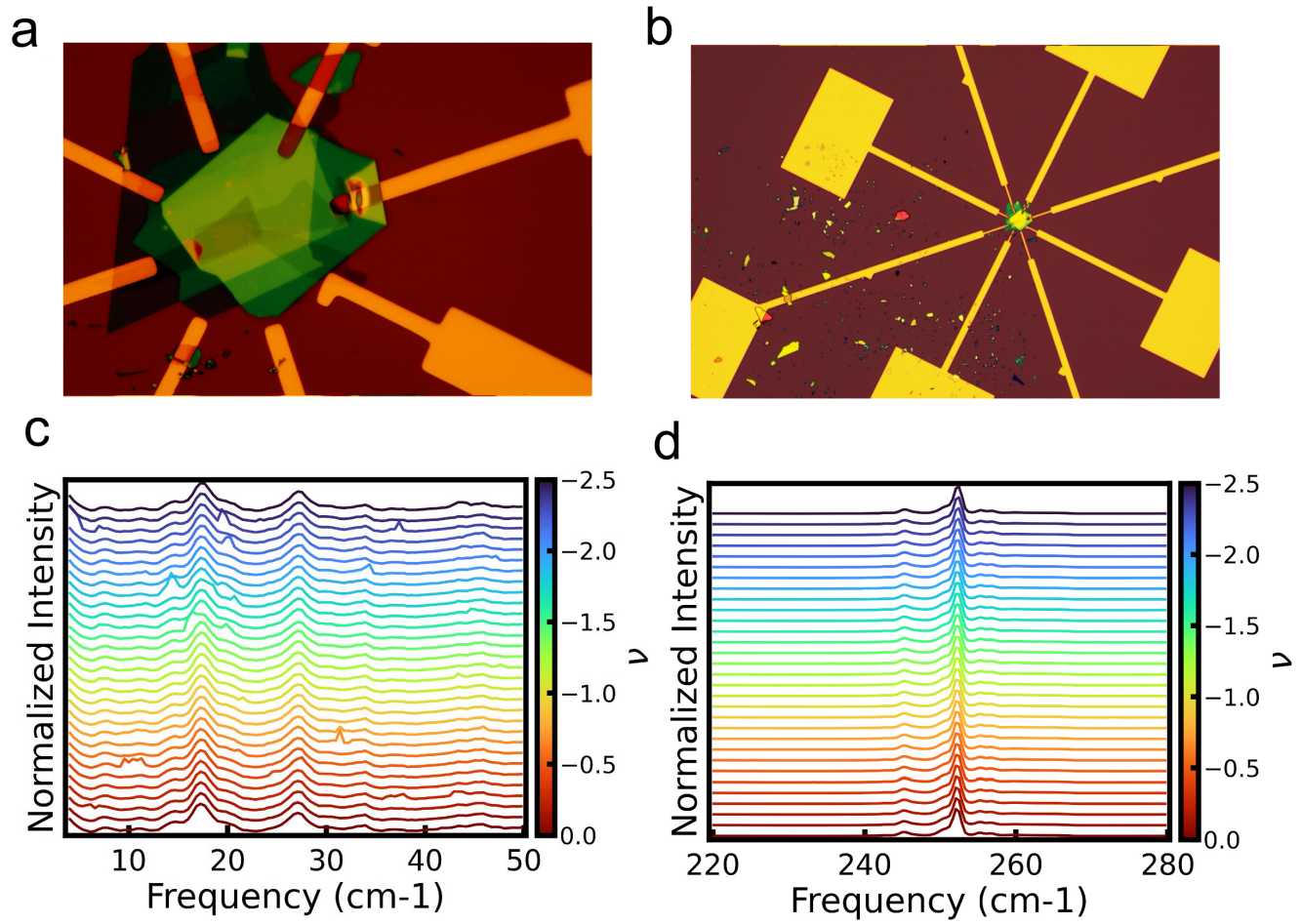

FIG. S14. Raman characterization of the t-WSe_2 device with a twist angle of 3.15°. **a**, **b**, Optical microscope images of the device used for Raman measurements. **c**, Low-frequency Raman spectra at different filling factors. **d**, High-frequency Raman spectra at different filling factors.